Optimization of Magnetic Field Focusing and Null Steering for Selective Wireless Power Transfer

Haejoon Jung, *Member, IEEE*, and Byunghun Lee, *Member, IEEE*

***Abstract*—Wireless power transfer (WPT) has recently emerged as a prominent technology to liberate various applications with small devices from limited mobility and design constraints. Among various techniques, magnetic field focusing (MFF) with multiple transmit (Tx) coils have been known as a powerful solution to enhance the efficiency of power transfer to multiple receivers (Rxs) in midrange WPT. However, in such MFF techniques, even unintended Rx may suffer from unwanted power due to leakage, which may disrupt the operations of the devices. Motivated by this issue, in this article, we consider selective magnetic resonance coupling (MRC)-based WPT, which enables WPT systems to better shape power distribution only focusing on the intended Rxs while leakages to the unintended Rx are suppressed. To this end, we first formulate the selectivity requirement of WPT as an optimization problem. Then, we propose a method to obtain the optimal Tx voltage vector for simultaneous MFF and null-steering optimization. Simulation and experimental results validate the theoretical analysis and the proposed method in practical scenarios.**

***Index Terms*—Magnetic field focusing (MFF), magnetic resonance coupling (MRC), null steering, selective WPT, wireless power transmission (WPT).**

I. Introduction

WIRELESS power transfer (WPT) has been a very popular technology in various applications such as biomedical implants, electric vehicles, mobile devices, and Internet of things (IoT) due to the convenience of wireless charging without the physical contacts [1]–[5]. Recently, the wireless charging technique has been developed for the multiple receivers (Rxs) in the wireless charging platform [6]–[8], evolved from the conventional WPT technologies, which are mainly interested in the wireless charging between single transmitter (Tx) and Rx [2]–[5]. The wireless charging platform for the multiple devices would bring a great convenience to the users eliminating the messy wires and reducing the size of batteries in the biomedical or wireless mobile applications.

Manuscript received April 14, 2019; revised June 23, 2019 and July 27, 2019; accepted September 3, 2019. Date of publication September 10, 2019; date of current version February 11, 2020. This work was supported by the National Research Foundation of Korea under Grants NRF-2019R1F1A1047989 and NRF-2017R1C1B5076814 funded by the Korea Government. Recommended for publication by Associate Editor J. Acero. *(Corresponding author: Byunghun Lee.)*

H. Jung is with the Department of Information and Telecommunication Engineering, Incheon National University, Incheon, South Korea (e-mail: haejoonjung@inu.ac.kr).

B. Lee is with the Department of Electrical Engineering, Incheon National University, Incheon 22012, South Korea (e-mail: byunghun_lee@inu.ac.kr).

Color versions of one or more of the figures in this article are available online at http://ieeexplore.ieee.org.

Digital Object Identifier 10.1109/TPEL.2019.2940739

Even though several wireless charging platforms have been investigated for improving the charging efficiency and wireless coverage [9]–[11], there have been few wireless charging platforms focused on the selective power transfer for multiple Rxs compared to the selective data transmission (i.e., information security) for multiple Rxs, which has been an extensively studied topic in communications. While the selective data transmission can be achieved by the encrypted message that allows the specific users to decode the transmitted information with decryption keys, wirelessly transmitted energy can neither be encrypted nor authenticated to guarantee confidentiality of charging specific devices [12]. This makes power transfer channels vulnerable to attacks that threaten the safety or disrupt the operations of devices [13]–[15]. For example, passive backscattering tags might be mistakenly awakened by undesirable leakage from WPT systems. To tackle such issues, the selectivity of WPT should ensure efficient energy transfer only to intended receivers while preventing energy leakage to unintended receivers, which is referred to as *power security* in [16].

Considering its significance, the leakage control (i.e., selectivity) should be an integral part of any practical WPT applications, especially in safety critical or high device density scenarios. When it comes to magnetic resonance coupling (MRC)-based systems for midrange WPT, two approaches have been employed to improve the selectivity: adaptive carrier frequency and magnetic field focusing (MFF). The adaptive carrier frequency-based approach refers to techniques to achieve selectivity by adjusting the resonant characteristics, as in [17]–[21]. For example, in [21], the authors considered a frequency tuning technique to optimize the system efficiency and suppress undesirable leakage in WPT systems with the multicoil transmitter. However, this adaptive carrier frequency approach increases the complexity of system due to the additional capacitor banks and data link between Tx and Rx to change the carrier frequency in transient. Especially, the Rx cannot receive any power when the Rx is completely turned off. Furthermore, the frequency tuning may violate the allowable bandwidths defined by regulations [22].

On the other hand, the MFF schemes enable the selective energy transfer by adjusting Tx source voltages (or equivalently currents) such that their induced magnetic fields are coherently combined at the desired receivers while destructively combined at the unintended receivers. Conventionally, MFF has been used to enhance the receiver power at a single receiver or multiple receivers without considering the power selectivity (or leakage control), as in [7], [8], and [23]–[31]. In other words, these techniques only focused on power transfer to the intended

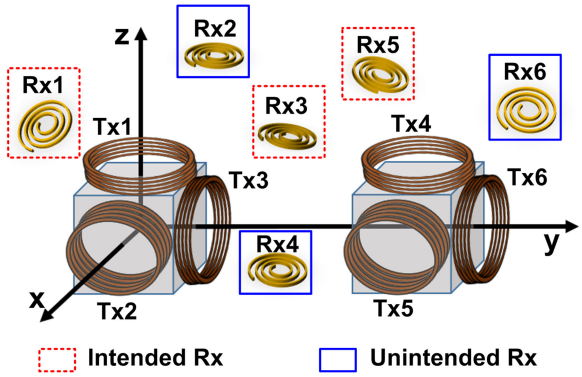

Fig. 1. Conceptual view of power selectivity system for distributed Rxs in the 3-D space. The proposed algorithm Tx coil array (Tx1–Tx6) maximizes the aggregate received powers at the intended Rxs with minimum power threshold to each, while it suppresses the unwanted leakages to the untended Rxs.

devices in the absence of any unintended devices, which may cause unwanted magnetic field exposure to adjacent devices in practice. Therefore, such MFF schemes proposed in [7], [8], and [23]–[31] are not pertinent to suppress undesirable leakages and guarantee selective WPT. To overcome this issue, selective WPT algorithms based on multicoil Tx have been proposed in [16] and [32]. However, they focused on the theoretical analysis without addressing implementation and experimentation for validation. In addition, their system models ignored mutual coupling between multiple receivers, which has limited applicability in practice. On the other hand, Waters *et al.* [22] demonstrated their leakage field control algorithm, but did not provide a detailed theoretical framework to optimize the MRC precoding vector, which is the key to achieve selective energy distributions.

In this article, we propose a novel selective WPT algorithm based on magnetic field focusing and null-steering optimization (MFFNSO) for MRC-based systems as shown in Fig. 1, where the intended and unintended Rxs are arbitrarily distributed in the three-dimensional (3-D) space. To overcome the issues and limitations in the existing studies, we consider more generalized scenarios to simultaneously support multiple intended Rxs in the presence of multiple unintended Rxs without any approximation for simplicity. In addition, this article provides both analytical and experimental aspects of the selective WPT to bridge the gap between the two. The rest of this article is organized as follows. The notations and system model are introduced in Section II. In Section III, the MFFNSO algorithm including the detailed method to obtain source voltages that guarantee the power selectivity is presented. In Section IV, we provide simulation and experimental results to evaluate the effectiveness of the proposed scheme, followed by discussions and conclusions in Sections V and VI, respectively.

II. Preliminaries

A. Notation

The notations in Table I are adopted throughout the article. We denote vectors and matrices by boldface lower case ($\boldsymbol{x}$) and upper case ($\boldsymbol{X}$), respectively. C^N and $C^{N\times N}$ means the set of N-dimensional and $N \times N$-dimensional complex-valued numbers. Also, $\|\cdot\|$ represents the absolute value operation, while $(\cdot)^T$ and $(\cdot)^H$ means the transpose and the conjugate transpose operators, respectively. The notation $\mathrm{tr}(\cdot)$ refers to the trace of the square matrix argument. We use diag$[\cdot]$ to denote a diagonal matrix with the given diagonal and zero off-diagonal entries. The curled inequality symbol $\succcurlyeq$ is used to indicate generalized inequality: $\boldsymbol{X} \succcurlyeq 0$ implies that $\boldsymbol{X}$ is a positive semidefinite matrix. $\boldsymbol{X}^{1/2}$ stands for the square root matrix when $\boldsymbol{X} \succcurlyeq 0$. $\mathrm{E}[\cdot]$ is the statistical expectation, and $\boldsymbol{x} \sim CN(\boldsymbol{\mu}, \boldsymbol{C})$ implies that the random vector $\boldsymbol{x}$ follows the circularly symmetric complex Gaussian distribution with mean vector of $\boldsymbol{\mu}$ and the covariance matrix of $\boldsymbol{C}$.

TABLE I
Notation and Symbols for MFFNSO Algorithm

Symbol	Definition/Explanation
N	Number of Tx coils
n	Tx coil index
Q	Number of Rxs
T	Number of intended Rxs
q	Rx index
ω	Angular frequency
$\boldsymbol{i}_{Tx}$	Tx current vector
$\boldsymbol{i}_{Rx}$	Rx current vector
$\boldsymbol{v}_{Tx}$	Tx voltage vector
$\boldsymbol{Z}_{Tx}$	Tx resistances and inter-Tx couplings
$\boldsymbol{Z}_{Rx}$	Rx resistances and inter-Rx couplings
$\boldsymbol{M}$	Tx-Rx couplings
$\boldsymbol{A}$	$j\omega\, \boldsymbol{Z}_{Rx}^{-1}\boldsymbol{M}$
$\boldsymbol{B}$	$(\boldsymbol{Z}_T + \omega^2 \boldsymbol{M}^T \boldsymbol{Z}_{Rx}^{-1}\boldsymbol{M})$
$\boldsymbol{C}$	$(\sum_{q=1}^{T} \sqrt{R_{L,q}}\, \boldsymbol{W}_q)\, \boldsymbol{A}$
$\boldsymbol{Y}_q$	$\left(\sqrt{R_{L,q}}\, \boldsymbol{W}_q \boldsymbol{A}\right)^H \left(\sqrt{R_{L,q}}\, \boldsymbol{W}_q \boldsymbol{A}\right)$
P_s	Total power consumption threshold
P_n	Power threshold of Tx n
Γ_q	Maximum load power threshold at an unintended Rx q
κ_q	Minimum load power threshold at an intended Rx q
V_n	Maximum voltage of voltage source at Tx n

B. System Model

As shown in Fig. 2, we consider a WPT system with a transmitter, which is equipped with N transmit coils (Txs), and Q receivers (Rxs) with a single coil each. Each Tx has a power source supplying sinusoidal voltage, which is denoted by a complex variable $v_{\mathrm{Tx},n}$, and the corresponding current is denoted by $i_{\mathrm{Tx},n}$ for $n = 1, \ldots, N$. Among the Q receivers, there are T target (intended) receivers, the aggregate received power of which needs to be maximized, while each has a certain minimum received power requirement. On the other hand, the other $Q - T$ receivers are unintended receivers to which the power leakage should be suppressed. To satisfy this goal, MFFNSO is exploited, where both amplitudes and phases of the transmitter voltages $v_{\mathrm{Tx},n}$ are adjusted. To be specific, the total received power at the desired receiver, i.e., Rx 1 to T, needs to be maximized,

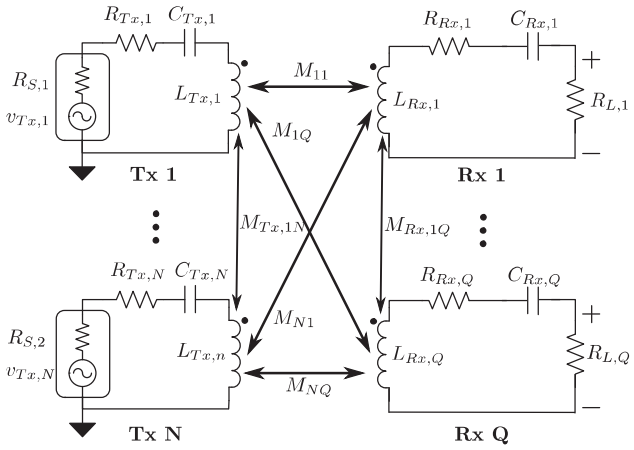

Fig. 2. Lumped circuit models of a magnetic field control system with multiple transmit and receive coils.

while at the same time the received power at the other receivers, i.e., Rx $T+1$ to Q, should be kept below a certain threshold Γ_q. As a part of resonant circuit, the inductance and capacitance at Tx n are chosen so that their impedances are canceled each other as

$$j\omega L_{\mathrm{Tx},n} + \frac{1}{j\omega C_{\mathrm{Tx},n}} = 0 \tag{1}$$

where $n \in \{1, \ldots, N\}$. Similarly, at the qth receiver, it satisfies

$$\omega L_{\mathrm{Rx},q} + \frac{1}{j\omega C_{\mathrm{Rx},q}} = 0 \tag{2}$$

where $q \in \{1, \ldots, Q\}$. In addition, as in [16], [22], and [32], we assume that the mutual inductance between any pair of coils is available to the transmitter. We will discuss how to obtain this information in Section II-C in detail.

C. Circuit Equations

For Rx coil q, Kirchhoff's voltage law gives

$$z_{\mathrm{Rx},q} i_{\mathrm{Rx},q} + \underbrace{j\omega \sum_{\substack{l=1 \\ l\neq q}}^{Q} M_{\mathrm{Rx},ql} i_{\mathrm{Rx},l}}_{\text{from the other Rxs}} = \underbrace{j\omega \sum_{n=1}^{N} M_{nq} i_{\mathrm{Tx},n}}_{\text{from the Txs}} \tag{3}$$

where

$$z_{\mathrm{Rx},q} = R_{\mathrm{Rx},q} + R_{L,q} \tag{4}$$

based on the resonance condition in (2). On the other hand, the circuit equation for Tx n is given by

$$v_{\mathrm{Tx},n} = z_{\mathrm{Tx},n}\, i_{\mathrm{Tx},n} + \underbrace{j\omega \sum_{\substack{m=1 \\ m\neq n}}^{n} M_{\mathrm{Tx},nm} i_{\mathrm{Tx},m}}_{\text{from the other Txs}} - \underbrace{j\omega \sum_{q=1}^{m} M_{nq} i_{\mathrm{Rx},q}}_{\text{from the Rxs}} \tag{5}$$

where $z_{\mathrm{Tx},n} = R_{s,n} + R_{\mathrm{Tx},n}$. Based on (4) and (5), the matrix form of simultaneous equations can be represented as

$$\boldsymbol{i}_{\mathrm{Rx}} = j\omega \boldsymbol{Z}_{\mathrm{Rx}}^{-1} \boldsymbol{M} \boldsymbol{i}_{\mathrm{Tx}} = \boldsymbol{A} \boldsymbol{i}_{\mathrm{Tx}} \tag{6}$$

$$\boldsymbol{v}_{\mathrm{Tx}} = \left(\boldsymbol{Z}_T + \omega^2 \boldsymbol{M}^T \boldsymbol{Z}_{\mathrm{Rx}}^{-1} \boldsymbol{M}\right) \boldsymbol{i}_{\mathrm{Tx}} = \boldsymbol{B} \boldsymbol{i}_{\mathrm{Tx}} \tag{7}$$

where $\boldsymbol{i}_{\mathrm{Tx}} = [i_{\mathrm{Tx},1}, \ldots, i_{\mathrm{Tx},N}]^T$, $\boldsymbol{i}_{\mathrm{Rx}} = [i_{\mathrm{Rx},1}, \ldots, i_{\mathrm{Rx},Q}]^T$, and $\boldsymbol{v}_{\mathrm{Tx}} = [v_{\mathrm{Tx},1}, \ldots, v_{\mathrm{Tx},N}]^T$. Also, $\boldsymbol{A} = j\omega \boldsymbol{Z}_{\mathrm{Rx}}^{-1} \boldsymbol{M}$, and $\boldsymbol{B} = (\boldsymbol{Z}_T + \omega^2 \boldsymbol{M}^T \boldsymbol{Z}_{\mathrm{Rx}}^{-1} \boldsymbol{M})$, where $\boldsymbol{M}$ indicates the Tx–Rx mutual coupling matrix as

$$\boldsymbol{M} = \begin{bmatrix} M_{11} & \cdots & M_{N1} \\ \vdots & \ddots & \vdots \\ M_{1Q} & \cdots & M_{NQ} \end{bmatrix}. \tag{8}$$

Also, the transmitter and receiver impedance matrices, $\boldsymbol{Z}_{\mathrm{Tx}}$ and $\boldsymbol{Z}_{\mathrm{Rx}}$, are given by

$$\boldsymbol{Z}_{\mathrm{Tx}} = \begin{bmatrix} z_{\mathrm{Tx},1} & j\omega M_{\mathrm{Tx},12} & \cdots & j\omega M_{\mathrm{Tx},1N} \\ j\omega M_{\mathrm{Tx},21} & z_{\mathrm{Tx},2} & \cdots & j\omega M_{\mathrm{Tx},2N} \\ \vdots & \vdots & \ddots & \vdots \\ j\omega M_{\mathrm{Tx},N1} & j\omega M_{\mathrm{Tx},N2} & \cdots & z_{\mathrm{Tx},N} \end{bmatrix} \tag{9}$$

$$\boldsymbol{Z}_{\mathrm{Rx}} = \begin{bmatrix} z_{\mathrm{Rx},1} & j\omega M_{\mathrm{Rx},12} & \cdots & j\omega M_{\mathrm{Rx},1Q} \\ j\omega M_{\mathrm{Rx},21} & z_{\mathrm{Rx},2} & \cdots & j\omega M_{\mathrm{Rx},2Q} \\ \vdots & \vdots & \ddots & \vdots \\ j\omega M_{\mathrm{Rx},Q1} & j\omega M_{\mathrm{Rx},Q2} & \cdots & z_{\mathrm{Rx},Q} \end{bmatrix}. \tag{10}$$

As a result, the power delivered to load (PDL) of Rx q is expressed as

$$p_{\mathrm{Rx},q} = \frac{1}{2} R_{L,q} |i_{\mathrm{Rx},q}|^2. \tag{11}$$

Similarly, the power dissipated at Tx n is given by

$$p_{\mathrm{Tx},n} = \frac{1}{2} z_{\mathrm{Tx},n} |i_{\mathrm{Tx},n}|^2. \tag{12}$$

Consequently, the total power consumed in the entire system including all of the Txs and Rxs is given by

$$\begin{aligned} p_S &= \sum_{n=1}^{N} p_{\mathrm{Tx},n} + \sum_{q=1}^{Q} \left(p_{\mathrm{Rx},q} + \frac{1}{2} R_{\mathrm{Rx},q} |i_{\mathrm{Rx},q}|^2 \right) \\ &= \frac{1}{2} \boldsymbol{i}_{\mathrm{Tx}}^H \left(\boldsymbol{R}_{\mathrm{Tx}} + \boldsymbol{A}^H \boldsymbol{R}_{\mathrm{Rx}} \boldsymbol{A} \right) \boldsymbol{i}_{\mathrm{Tx}} \end{aligned} \tag{13}$$

where $\boldsymbol{R}_{\mathrm{Tx}} = \mathrm{diag}\{z_{\mathrm{Tx},1}, \ldots, z_{\mathrm{Tx},N}\}$ and $\boldsymbol{R}_{\mathrm{Rx}} = \mathrm{diag}\{R_{L,1} + R_{\mathrm{Rx},1}, \ldots, R_{L,Q} + R_{\mathrm{Rx},Q}\}$.

We assume that both intended and unintended groups of Rxs share their measured currents as well as the Rx resistances, since each Rx can estimate its own resistance a priori. This condition can be satisfied when the unintended Rxs are also registered users of the WPT system, but they need to be protected from unwanted leakage. In contrast, in case that the unintended Rxs are malicious, and they report manipulated values, which are different from their actual measured currents, it is difficult to collect their exact magnetic channel state information.

However, the Tx can at least identify such manipulation by checking the relationship between Tx voltages and Tx currents using (7), as noted in [29]. The extension to selective WPT in the absence of the mutual inductances and resistances of the unintended Rxs, which may be a realistic assumption in power security against theft of electricity considered in [15] and [32], is deferred to future work. Furthermore, we will discuss how to formulate the optimization problem of the selective WPT and collect the required information to solve it in the next section.

III. MFFNSO for Selective WPT

In this section, we discuss how to determine the optimal Tx voltage vector, $\boldsymbol{v}_{\mathrm{Tx}}^{*}$ [or equivalently the optimal Tx current vector $\boldsymbol{i}_{\mathrm{Tx}}^{*}$ using (7)] that maximizes the sum of the received powers at the desired receivers while suppressing the received powers at the other receivers below the given threshold Γ_q. We first formulate the optimization problem and then introduce the proposed approach using semidefinite relaxation (SDR), which has been known as a powerful and computationally efficient technique for a host of very difficult optimization problems in the area of signal processing and communications [33].

A. Problem Formulation

Our problem of interest is to maximize the sum of the load powers at the desired Rxs, $\sum_{q=1}^{T} p_{\mathrm{Rx},q}$, under the following constraints: the total power dissipation of the system needs to be smaller than or equal to P_S, i.e., $p_S \leq P_s$; the power consumed at each Tx should be smaller than or equal to P_n, i.e., $p_{\mathrm{Tx},n} \leq P_n$; the peak amplitude of each Tx voltage needs to be no larger than a certain threshold V_n, i.e., $|v_{\mathrm{Tx},n}| \leq V_n$ for $n = 1, \ldots, N$. At the same time, the load power at each of the unintended Rxs should be kept no larger than the given threshold Γ_q, i.e., $p_{\mathrm{Rx},q} \leq \Gamma_q$ for $q = T+1, \ \ldots, \ Q$. In addition, the load power at each of the intended Rxs should be greater than or equal to the minimum power requirement value κ_q, i.e., $p_{\mathrm{Rx},q} \geq \kappa_q$ for $q = 1, \ \ldots, T$. This problem can be formulated as follows:

$$(\mathrm{P0}): \max_{\boldsymbol{i}_{\mathrm{Tx}} \in C^N} \frac{1}{2} \boldsymbol{i}_{\mathrm{Tx}}^{H} \boldsymbol{C}^{H} \boldsymbol{C} \boldsymbol{i}_{\mathrm{Tx}} \tag{14a}$$

$$\text{s.t. } p_{\mathrm{Tx},n} \leq P_n, \quad n = 1, \ldots, N \tag{14b}$$

$$p_{\mathrm{Rx},q} \leq \Gamma_q, \quad q = T+1, \ldots, Q \tag{14c}$$

$$p_{\mathrm{Rx},q} \geq \kappa_q, \quad q = 1, \ldots, T \tag{14d}$$

$$p_S \leq P_S \tag{14e}$$

$$|v_{\mathrm{Tx},n}| \leq V_n \tag{14f}$$

where $\boldsymbol{C} = (\sum_{q=1}^{T} \sqrt{R_{L,q}} \boldsymbol{W}_q) \boldsymbol{A}$ with $\boldsymbol{W}_q$ being a $Q \times Q$ matrix as

$$\boldsymbol{W}_q(u, v) = \begin{cases} 1, & u = v = q \\ 0, & \text{otherwise.} \end{cases} \tag{15}$$

By solving (P0), the optimum precoding current vector $\boldsymbol{i}_{\mathrm{Tx}}^{*}$ is obtained, and the corresponding voltage can be readily calculated from (7).

We note that (P0) is a nonconvex quadratically constrained quadratic problem (QCQP), which belongs to the class of nondeterministic polynomial-time hardness (NP-hard) problems, and it is thus difficult to solve in general. For this reason, in Section III-B, we will transform this nonconvex QCQP problem into a linear optimization problem via SDR [33] followed by a postprocessing procedure.

B. Semidefinite Relaxation

The first step in obtaining an SDR of (P0) is to define a rank-one matrix $\boldsymbol{X} = \boldsymbol{i}_{\mathrm{Tx}} \boldsymbol{i}_{\mathrm{Tx}}^{H} \succcurlyeq 0$. Introducing this new variable, we obtain the following formulation, which is equivalent to (P0):

$$(\mathrm{P1}): \max_{\boldsymbol{X} \in C^{N \times N}} \mathrm{tr}\left(\boldsymbol{C}^{H} \boldsymbol{C} \boldsymbol{X}\right) \tag{16a}$$

$$\text{s.t. } \mathrm{tr}\left(\boldsymbol{R}_{\mathrm{Tx}} \boldsymbol{\Sigma}_n \boldsymbol{X}\right) \leq 2P_n, \quad n = 1, \ldots, N \tag{16b}$$

$$\mathrm{tr}\left(\boldsymbol{Y}_{\boldsymbol{q}} \boldsymbol{X}\right) \leq 2\Gamma_q, \quad q = T+1, \ldots, Q \tag{16c}$$

$$\mathrm{tr}\left(\boldsymbol{Y}_{\boldsymbol{q}} \boldsymbol{X}\right) \geq 2\kappa_q, \quad q = 1, \ldots, T \tag{16d}$$

$$\mathrm{tr}\left(\left(\boldsymbol{R}_{\mathrm{Tx}} + \boldsymbol{A}^{H} \boldsymbol{R}_{\mathrm{Rx}} \boldsymbol{A}\right) \boldsymbol{X}\right) \leq P_S \tag{16e}$$

$$\mathrm{tr}\left(\boldsymbol{B}^{\boldsymbol{H}} \boldsymbol{\Sigma}_n \boldsymbol{B} \boldsymbol{X}\right) \leq V_n^2 \tag{16f}$$

$$\boldsymbol{X} \succcurlyeq 0 \tag{16g}$$

$$\mathrm{rank}\left(\boldsymbol{X}\right) = 1 \tag{16h}$$

where $\boldsymbol{\Sigma}_n$ is an $N \times N$ matrix with nth orthogonal element being one and others zero. Also $\boldsymbol{Y}_q = (\sqrt{R_{L,q}} \boldsymbol{W}_q \boldsymbol{A})^{H} (\sqrt{R_{L,q}} \boldsymbol{W}_q \boldsymbol{A})$.

In fact, it is as difficult to solve as (P0). However, (P1) without the rank-one constraint in (16h), which is known as SDR of (P1), is possible to solve, to any arbitrary accuracy, in a numerically reliable and efficient manner through convex optimization tools such as CVX [34]. However, in general, the solution $\boldsymbol{X}^{*}$ of (SDR-P1) may not be a rank-one matrix. Hence, to handle this issue, we present a method to achieve an approximate solution in the following section.

It is noted that this optimization problem formulation given in (P0) or (P1) is appropriate for the situations, where the received powers (or unwanted leakages) at the unintended Rxs should be kept below a certain threshold Γ_q to safeguard the devices (i.e., unintended Rxs). In this article, we focus on this scenario. However, for some applications (e.g., power security against theft of electricity), the ratio between the received powers of the intended and unintended receivers is more important. Especially, if the total power consumption threshold at Tx P_S and the maximum voltage level of the individual voltage source V_n are high enough, it is more critical to provide higher power to the intended Rxs compared to the unintended Rxs by maximizing the ratio between the received power sums (or weighted sums depending on priorities) of the two groups. Unfortunately, maximizing this ratio is a nonconvex optimization problem, which cannot be solved by well-known tools of convex optimization such as CVX. Instead, we can consider the iterative approach as proposed in [27].

TABLE II
PROPOSED MFFNSO ALGORITHM BY RANDOMIZATION

Input: $\boldsymbol{A}, \boldsymbol{B}, \boldsymbol{C}, \boldsymbol{R}_{Tx}, \boldsymbol{R}_{Rx}$,
Output: a solution $\boldsymbol{x}^*$
1: Solve the (SDR-P1) in (16) finding $\boldsymbol{X}^*$; evaluate $\rho = \text{rank}(\boldsymbol{X}^*)$
2: **if** $\rho = 1$ **then**
3: $\quad \boldsymbol{x}^* = \sqrt{\lambda_1}\boldsymbol{u}_1$
4: **else**
5: $\quad$ **for** $\ell = 1, \ldots, L$
6: $\quad\quad$ generate a random vector $\boldsymbol{x}_\ell = \boldsymbol{U}\boldsymbol{\Lambda}^{1/2}\boldsymbol{\xi}_\ell$, where $\boldsymbol{\xi}_\ell \sim CN(\boldsymbol{0}_N, \boldsymbol{I}_N)$, and construct a feasible point $\widetilde{\boldsymbol{x}}_\ell$
7: $\quad$ **end for**
8: $\quad \boldsymbol{x}^* = \underset{\widetilde{\boldsymbol{x}}_\ell}{\text{argmax}}\, \widetilde{\boldsymbol{x}}_\ell^{\boldsymbol{H}} \boldsymbol{C}^H \boldsymbol{C} \widetilde{\boldsymbol{x}}_\ell$
9: **end if**
10: **return** $\boldsymbol{x}^*$

C. Rank-Reduction Procedure

A classical way to retrieve a rank-one optimal solution from the SDR is the rank-reduction procedure, as noted in [35]. The simplest rank reduction technique is the eigenvector approximation as follows. Suppose that $\rho = \text{rank}(\boldsymbol{X}^*)$, and let

$$\boldsymbol{X}^* = \boldsymbol{U}\boldsymbol{\Lambda}\boldsymbol{U}^H = \sum_{n=1}^{\rho} \lambda_n u_n u_n^H \tag{17}$$

be the eigenvalue decomposition of $\boldsymbol{X}^*$, where $\boldsymbol{\Lambda} = \text{diag}\{\lambda_1, \ldots, \lambda_N\}$, where $\lambda_1 \geq \lambda_2 \geq \cdots \geq \lambda_\rho > 0$ are eigenvalues and $u_1, \ldots, u_n$ are the respective eigenvectors. Thus, the rank-one approximation can be given by $\boldsymbol{X}_1^* = \lambda_1 \boldsymbol{u}_1 \boldsymbol{u}_1^H$, and $\widetilde{\boldsymbol{i}}^* = \sqrt{\lambda_1}\boldsymbol{u}_1$ can be a candidate solution to (P0), as long as it suffices the given constraints from (14b) to (14f). If $\widetilde{\boldsymbol{i}}^*$ violates certain constrains, we can try map $\widetilde{\boldsymbol{i}}^*$ to a nearby feasible solution.

Unfortunately, this method provides an accurate approximation only when λ_1 is significantly greater than the other nonzero eigenvalues. In other words, it does not necessarily guarantee the global optimality of the extracted solution. For this reason, we consider the following randomized postprocessing procedure, which is widely used to better optimize the radio frequency (RF) beamforming systems, as in [26] and [35]. For a given number of randomizations L, the proposed MFFNSO algorithm is summarized as Table II.

D. Magnetic Channel Estimation

For implementation of the proposed algorithm, MFFNSO, we need to identify the matrices used in the optimization problem (P1). Table III provides the required information in each equation of (P1). In summary, to formulate the optimization problem in (P1), the Tx needs to know $\boldsymbol{W}_q$, $\boldsymbol{\Sigma}_n$, $\boldsymbol{R}_{\text{Tx}}$, $\sqrt{R_{L,q}}$, $\boldsymbol{R}_{\text{Rx}}$, $\boldsymbol{A}$, and $\boldsymbol{B}$. Because $\boldsymbol{W}_q$ and $\boldsymbol{\Sigma}_n$ are deterministic matrices, where all the elements are either zero or one, they do not need to be estimated. Furthermore, $\boldsymbol{R}_{\text{Tx}}$ (or $\boldsymbol{Z}_{\text{Tx}}$) is determined only by transmitter-specific parameters, it can be estimated *a priori* in a factory setting [29]. Also, as noted in the previous section, $\sqrt{R_{L,q}}$ and $\boldsymbol{R}_{\text{Rx}}$, which are functions of Rx resistances, can be reported by

TABLE III
MATRICES TO ESTIMATE IN (P1)

Equations	Required Information
(16a)	$\boldsymbol{C} \rightarrow \boldsymbol{A}, \boldsymbol{W}_q, \sqrt{R_{L,q}}$
(16b)	$\boldsymbol{\Sigma}_n,\ \boldsymbol{R}_{Tx}$
(16c)	$\boldsymbol{Y}_q \rightarrow \boldsymbol{A}, \boldsymbol{W}_q, \sqrt{R_{L,q}}$
(16d)	$\boldsymbol{Y}_q \rightarrow \boldsymbol{A}, \boldsymbol{W}_q, \sqrt{R_{L,q}}$
(16e)	$\boldsymbol{R}_{Tx}, \boldsymbol{R}_{Rx}, \boldsymbol{A}$
(16f)	$\boldsymbol{\Sigma}_n, \boldsymbol{B}$
(16g)	-
(16h)	-

the Rxs to the Tx array, since we assume all the receivers are registered users. To be specific, following [26] and [28], it is assumed that each RX feeds back its resistance information and measured current to the Tx by using its communication module. Thus, through this feedback, $\sqrt{R_{L,q}}$ and $\boldsymbol{R}_{\text{Rx}}$ can be obtained at the Tx. As a result, the remaining matrices for the Tx to estimate are $\boldsymbol{A}$and $\boldsymbol{B}$.

As defined in Table I, $\boldsymbol{A}$ and $\boldsymbol{B}$ are decomposed into $j\omega \boldsymbol{Z}_{\text{Rx}}^{-1}\boldsymbol{M}$ and $\boldsymbol{Z}_T + \omega^2 \boldsymbol{M}^T \boldsymbol{Z}_{\text{Rx}}^{-1}\boldsymbol{M}$, respectively. However, we do not need to estimate the individual matrices (i.e., $\boldsymbol{Z}_{\text{Rx}}$, $\boldsymbol{Z}_T$, and $\boldsymbol{M}$). Rather, it takes less time to estimate $\boldsymbol{A}$ and $\boldsymbol{B}$ as wholes, as suggested in [29]. First, to estimate $\boldsymbol{B}$, the equation in (7) can be rewritten as $\boldsymbol{v}_{\text{Tx}} = \boldsymbol{B}\boldsymbol{i}_{\text{Tx}}$, where $\boldsymbol{v}_{\text{Tx}}$ and $\boldsymbol{i}_{\text{Tx}}$ correspond to the Tx voltages and currents. Therefore, the two can be measured within the Tx without communication with the Rxs. Further, the coefficients between the two vectors can be readily identified by measuring the transmit current vector $\boldsymbol{i}_{\text{Tx}}$ after applying a random test voltage vector $\boldsymbol{v}_{\text{Tx}}$ without zero entry. Because $\boldsymbol{v}_{\text{Tx}}$ and $\boldsymbol{i}_{\text{Tx}}$ are vectors of length N, which is the number of the Tx coils, the Tx has to repeat such test measurements of the Tx currents $\boldsymbol{i}_{\text{Tx}}$ N times with N different sets of voltages $\boldsymbol{v}_{\text{Tx}}$. Then, as noted in [29], the matrix $\boldsymbol{B}$ can be estimated as

$$\boldsymbol{B} = \left[\boldsymbol{v}_{\text{Tx}}^{(1)}, \boldsymbol{v}_{\text{Tx}}^{(2)}, \ldots, \boldsymbol{v}_{\text{Tx}}^{(N)}\right] \left[\boldsymbol{i}_{\text{Tx}}^{(1)}, \boldsymbol{i}_{\text{Tx}}^{(2)}, \ldots, \boldsymbol{i}_{\text{Tx}}^{(N)}\right]^{-1} \tag{18}$$

where the superscript indicates the measurement index. In other words, $\boldsymbol{v}_{\text{Tx}}^{(n)}$ and $\boldsymbol{i}_{\text{Tx}}^{(n)}$ represent the Tx voltage and current vectors of the nth measurement, where $n = 1, \ldots, N$.

Similarly, we can estimate $\boldsymbol{A}$ based on the equation in (6), which is given by $\boldsymbol{i}_{\text{Rx}} = \boldsymbol{A}\boldsymbol{i}_{\text{Tx}}$. Once $\boldsymbol{B}$ is identified as in (18), the Tx current vector $\boldsymbol{i}_{\text{Tx}}$ can be adjusted by the Tx voltage vector $\boldsymbol{v}_{\text{Tx}}$. Thus, we can apply an arbitrary nonzero Tx current vector $\boldsymbol{i}_{\text{Tx}}$ and collect the Rx current information $\boldsymbol{i}_{\text{Rx}}$ through the feedback signals from the Rxs. By repeating this N times with N different $\boldsymbol{i}_{\text{Tx}}$, we can estimate the matrix $\boldsymbol{A}$ as

$$\boldsymbol{A} = \left[\boldsymbol{i}_{\text{Rx}}^{(1)}, \boldsymbol{i}_{\text{Rx}}^{(2)}, \ldots, \boldsymbol{i}_{\text{Rx}}^{(N)}\right] \left[\boldsymbol{i}_{\text{Tx}}^{(1)}, \boldsymbol{i}_{\text{Tx}}^{(2)}, \ldots, \boldsymbol{i}_{\text{Tx}}^{(N)}\right]^{-1} \tag{19}$$

where the superscript represents the measurement index from 1 to N.

E. Practical Considerations

The selectivity of WPT is subject to the similarity of Tx–Rx coupling vectors between the intended and unintended Rxs. In other words, if two Rxs are closely located with the same orientation, which also gives higher inter-Rx coupling, it is difficult for the Txs to distinguish the two Rxs. In this case, the power transferred to the intended Rx decreases to meet the constraint on the received power of the unintended Rx, which is denoted by Γ_q. At the same time, compared to the conventional WPT, the total power consumption at the Txs becomes larger to satisfy the power selectivity requirement. Also, due to the highly correlated received powers of the two Rxs, as the constraint Γ_q decreases, the received power at the intended Rx is likely to vastly decrease. As an extreme case, if the intended and unintended Rxs have exactly the same Tx–Rx coupling vectors, which is highly unlikely in reality, the MFFNSO algorithm gives the feasible solution only when $\kappa_q = \Gamma_q$, which means that selective WPT is not feasible. As RF communication systems accommodate more number of antennas to improve the spatial resolution of MFF and enhance power selectivity [36], [37], one way to improve the selectivity in MRC-WPT is to employ more Tx coils, which increases the chances to obtain more degrees of freedom (DoF) and distinguishable coupling vectors between arbitrary Rxs at the expense of increased complexity and costs for more Txs with the drivers and coils [38]. We will present simulation results of the performance of MFFNSO limited by the spatial resolution of MFF in Section IV-C.

Moreover, when it comes to a practical scenario, the mobility of Rxs should be considered. While the inter-Tx coupling is constant with fixed Tx positions, which can be measured and stored in advance, Tx–Rx couplings, which determine $\boldsymbol{A}$ and $\boldsymbol{B}$ as given respectively in (7) and (8), are generally time varying, Thus, the WPT system requires a capability to keep track of the Rxs' movement. In addition, the Tx should detect a new Rx that comes into the coverage. To address this mobility issue, algorithms to periodically estimate magnetic channels and detect the presence of Rxs have been proposed in [7], [26], and [29]. As long as this period magnetic channel estimation is performed frequently enough, the Tx can respond fast enough not to cause major issues in WPT selectivity as well as system efficiency.

IV. Verifications

In this section, we evaluate the performance of the proposed selective WPT algorithm, MFFNSO, through electromagnetic (EM) and circuit simulations as well as experiments with various configurations.

A. Selective WPT With Two Rxs

In this section, we consider the selective WPT with the proof-of-concept 3-D Tx coil array with two randomly placed Rx coils, as shown in Fig. 3. The figure shows the experimental setup for MFFNSO with the 3-D Tx coil array (Tx1–Tx3) along with the x, y, and z axes and the two Rx coils (Rx1, Rx2). The Tx1 coil is placed at (0, 0, 100 mm) along with the *xy* plane, while the vertical coils (Tx2, Tx3) are placed on the *yz* and *xz* planes with 50 mm offset, which corresponds to Tx2 at (50, 0, 50 mm) and Tx3 at (0, 50, 50 mm), respectively. The Rx1 is placed at (10, 80, 120 mm) without angular misalignment (coil is parallel to the *xy* plane), and the Rx2 is placed at (110, 0, 110 mm) with 45° rotation based on the *y*-axis. Each helical Tx coil has five turns with 8.6 cm diameter and 2.5 mm pitch size. The individual Rx coil has four turns with 5 cm diameter. Both Tx and Rx coils are tuned at the carrier frequency, $f_p = 2$ MHz, with the series resonant capacitors. The coil geometries and key parameters are summarized in Table IV. Individual Tx coil was driven by three full-bridge inverters, which have the internal resistance, $R_S = 1.5\ \Omega$, and capability of adjusting the voltage vectors, $v_{Tx,1} - v_{Tx,3}$, based on the MFFNSO. The Rx load, R_L, is decided by 4.7 Ω with the parasitic inductance of 0.21 μH at 2 MHz frequency.

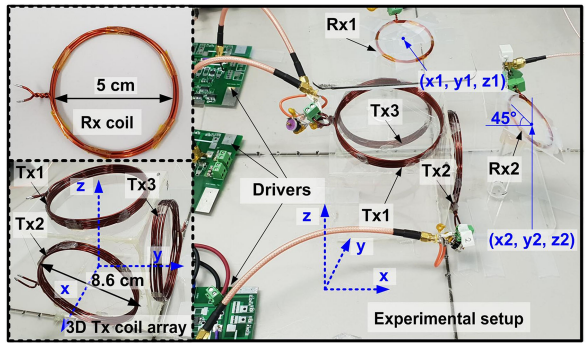

Fig. 3. Experimental setup for MFFNSO with the 3D Tx coil array (Tx1–Tx3) and two randomly distributed Rx coils (Rx1 and Rx2) in 3-D area. Tx1 is placed at (0, 0, 100 mm) along with the *xy* plane while the vertical coils (Tx2, Tx3) are placed on the *yz* and *xz* planes with 50 mm offset, respectively. Rx1 is placed at (10, 80, 120 mm) without angular misalignment, and Rx2 is placed at (110, 0, 110 mm) with the 45° angular misalignment from the *xy* plane.

TABLE IV
Coil Geometries of Test Setup

Parameters	Value
Wire-wound Helical Tx coils (Tx1 – Tx3)	Outer diameter = 8.6 cm Pitch = 2.5 mm Wire diameter = 1.628 mm Number of turns = 5 Inductance = 4.02 μH Resonance Cap. = 1.57 nF Quality factor = 159
Wire-wound Rx coils (Rx1 – Rx3)	Outer diameter = 5 cm Wire diameter = 0.812 mm Number of turns = 5 Inductance = 2.56 μH Resonance Cap. = 2.30 nF Quality factor = 101
Carrier frequency (f_p)	2 MHz
Loading (R_L)	4.7 Ω

In the experimental setup, two different scenarios are considered, which are 1) intended Rx1 and unintended Rx2, and 2) unintended Rx2 and intended Rx1, respectively, while the two Rx positions are fixed. The measured mutual inductance between Tx and Rx array is summarized in Table V, where the negative sign indicates 180° phase difference between two coils.

TABLE V
MEASURED MUTUAL INDUCTANCE BETWEEN TX AND RX ARRAYS

	Tx1	Tx2	Tx3	Rx1	Rx2	Rx3
Tx1	-	-0.2620*	0.2661	0.0642	-0.0125*	0.0116
Tx2	-0.2620*	-	0.2633	0.0175	0.0532	-0.0438*
Tx3	0.2661	0.2633	-	0.0805	0.0089	-0.0304*
Rx1	0.0642	0.0175	0.0805	-	-0.0032*	0.0001
Rx2	-0.0125*	0.0532	0.0089	-0.0032*	-	-0.0094*
Rx3	0.0116	-0.0438*	-0.0304*	0.0001	-0.0094*	-

*Negative sign indicates 180° phase difference (Unit: μH).

We note that Rx3 is not used in this experiment but is used in the experiment with three Rxs in Section IV-B. Based on the key parameters in Tables IV and V, the optimal Tx voltage vectors, $v_{Tx,1} - v_{Tx,3}$, can be calculated by MFFNSO in Table II to deliver the power to the intended Rx, while it limits the power to the unintended Rx. The limitation of power level for the unintended Rx and the maximum amplitude of Tx vectors are 5 mW and 5 V, respectively. For comparison, we also show the results of two other driving methods, which are maximum PDL and selective Tx driving among Tx1–Tx3. In the maximum PDL method, the amplitudes of $v_{Tx,1} - v_{Tx,3}$ are maximized but each phase is individually optimized through exhaustive search to achieve the maximum PDL to the intended Rx without any consideration of the unintended Rx. In the Tx selection method, on the other hand, a single Tx coil is only enabled with the maximum amplitude of 5 V. In Fig. 4, we present the power ratio of the intended and unintended Rx powers ($=P_{\text{intend}}/P_{\text{unintend}}$), which indicates the power selectivity between the two.

Assuming that the Rx1 is the intended and the Rx2 is unintended, the optimal Tx vectors for the three Tx coils, Tx1, Tx2, and Tx3, are 5sin(ωt) V, 2.2sin(ωt-6°) V, and 5sin(ωt-4°) V, respectively, as shown in Fig. 4. We note that the relative phase differences among the Tx coils are important for the selective WPT rather than the absolute values of the phases. In other words, adding the same phase offsets does not impact the results because the relative phase differences are kept to be the same. As shown in the figure, the resulted Rx1 and Rx2 powers are measured as 753 and 2.3 mW, respectively, which satisfies 5 mW limitation in the unintended Rx power and shows the power ratio of about 327. In this scenario, the overall system efficiency is measured as 29.9%, which is defined by the ratio between the sum of Rx powers (Rx1 + Rx2 powers) and sum of power consumption in three Txs including the inverter. Although the max PDL for Rx1 shows more received power in the Rx1 up to 810 mW with the increased system efficiency, 34.0%, the received power in the Rx2 rapidly increases to 72 mW resulting in the failure of 5 mW limitation and the poor power ratio of 11.

For the intended Rx2 and unintended Rx1, the optimal Tx voltage vectors from MFFNSO are 5sin(ωt) V, 5sin(ωt-197°) V, and 3.9sin(ωt-162°) V. It gives 3.4 mW and 239 mW of received Rx powers at Rx1 and Rx2 respectively, which suffices the 5 mW limitation at the Rx1. The overall system efficiency and power ratio are measured as 10.4% and 73, respectively. The max PDL for Rx2 is 245 mW with 12.3% system efficiency but the Rx1 power increased to 68 mW and the power ratio decreases to 3.6, which corresponds to low power selectivity. In both cases with the different intended Rxs, the efficiency of the max PDL is higher compared to the proposed MFFNSO algorithm. Furthermore, the delivered power to the intended Rx is also higher with the max PDL scheme compared to MFFNSO. It is because the selectivity of MFFNSO is achieved at the cost of efficiency (i.e., the Tx consumes more power for destructive combining at the unintended Rx), especially when 1) the unintended Rx is physically closer to the Tx compared to the intended Rx or 2) the magnetic channels of the intended and unintended Rxs are highly correlated (e.g., a small separation between the Rxs). Thus, in such cases, as the selectivity requirement becomes more stringent (i.e., Γ_q decreases), the efficiency gap between the proposed scheme and the max PDL algorithm may increase.

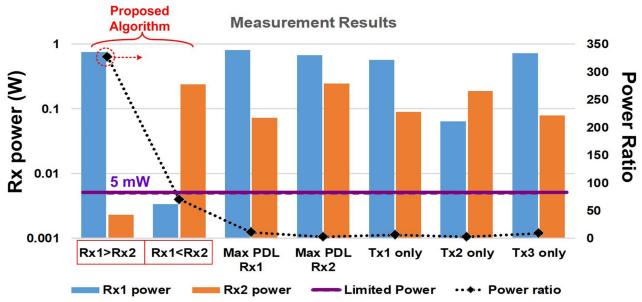

		Tx1	Tx2	Tx3		Rx1	Rx2
Proposed Algorithm (MFFNSO)	Intended Rx1	5 V (0°)	2.2 V (-6°)	5 V (-4°)	Mea.	753 mW	2.3 mW
					Sim.	534 mW	3.4 mW
	Intended Rx2	5 V (0°)	5 V (-197°)	3.9 V (-162°)	Mea.	3.4 mW	239 mW
					Sim.	4.3 mW	190 mW
Max PDL for Rx1		5 V (0°)	5 V (-3.1°)	5 V (-1.1°)	Mea.	810 mW	72 mW
					Sim.	610 mW	40 mW
Max PDL for Rx2		5 V (0°)	5 V (177°)	5 V (163°)	Mea.	68 mW	245 mW
					Sim.	40 mW	210 mW
Tx1 only		5 V (0°)	0 V	0 V	Mea.	570 mW	90 mW
					Sim.	370 mW	81 mW
Tx2 only		0 V	5 V (0°)	0 V	Mea.	64 mW	190 mW
					Sim.	27 mW	150 mW
Tx3 only		0 V	0 V	5 V (0°)	Mea.	730 mW	80 mW
					Sim.	580 mW	55 mW

Fig. 4. Simulated and measured Rx powers with the optimized Tx vectors, $v_{Tx,1}$–$v_{Tx,3}$, obtained by MFFNSO compared to the other feasible driving methods, which are maximum PDL and Tx selection among Tx1–Tx3.

Fig. 5(a) shows the EM simulation (FEKO [39]) model of the 3-D Tx coil array with two Rx coils same as the experimental setup in Fig. 3 and Table IV. Simulated results of the normalized H-field intensity are shown in Fig. 5(b) and (c) for 1) the intended Rx1/unintended Rx2 and 2) the unintended Rx1/intended Rx2 based on the optimized $v_{Tx,1} - v_{Tx,3}$ by the MFFNSO in Fig. 4. The simulated results clearly show that the optimized $v_{Tx,1} - v_{Tx,3}$ focus the H-field at the intended Rx while minimizing the H-field at the unintended Rx for two different scenarios, which are matched with the theoretical analysis and measurement results.

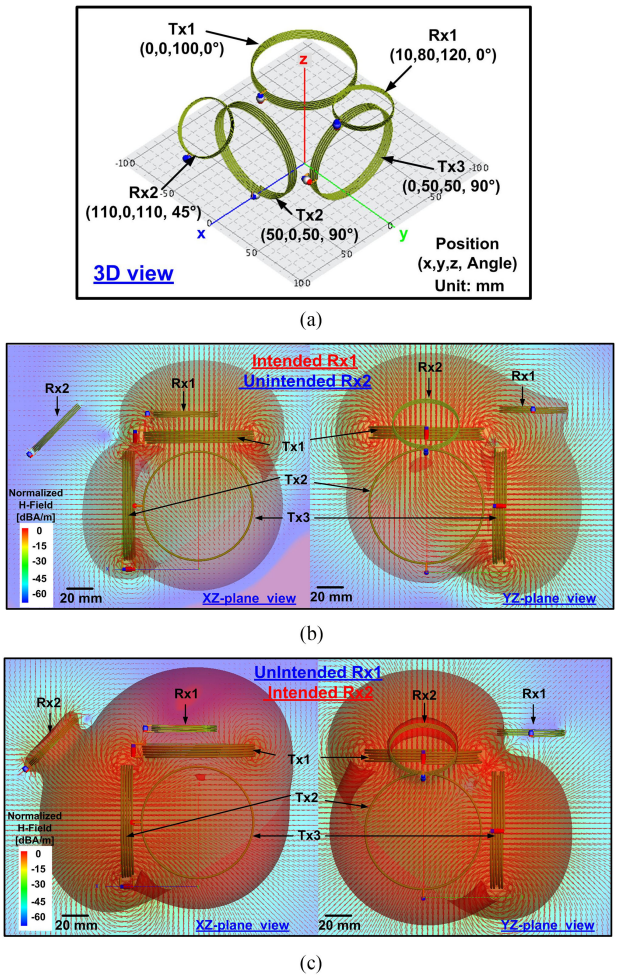

Fig. 5. (a) EM simulation model of the 3-D Tx coil array with two Rx coils, and the results of the normalized H-field intensity for (b) intended Rx1 and unintended Rx2 and (c) unintended Rx1 and intended Rx2 based on the MFFNSO algorithm. The arrows indicate the direction and magnitudes of the flux in the 3-D plot.

The measured transient waveforms for the Rx1 and Rx2 loads, $R_L = 4.7\ \Omega$, in two different scenarios are shown in Fig. 7. For the intended Rx1 and unintended Rx2 scenario, the received voltages at R_L are 2.66 and 0.15 V for the Rx1 and Rx2, respectively, resulting in 29.9% system efficiency as shown in Fig. 6(a). On the contrary, the received voltages at the Rx1 and Rx2 are 0.18 and 1.5 V, respectively, for the unintended Rx1 and intended Rx2 scenarios in Fig. 6(b), which has 10.4% system efficiency. The effectiveness of the proposed MFFNSO scheme with respect to the amplitude and phase variation from the optimal derived Tx vectors is further investigated for the unintended Rx1 and intended Rx2 scenario, as shown in Fig. 7. The amplitude and phase in the individual Tx coils are changed from 0 to 5 V, and $\pm 30°$, respectively, while the other Tx coils keep the optimal Tx vectors. Considering that MFFNSO is designed to find the optimal Tx vectors which delivers the maximum power to the intended Rx2 and limits the unintended Rx1 power under 5 mW constrains, Fig. 7 shows that the optimal derived Tx vectors are properly determined while satisfying the power constrains.

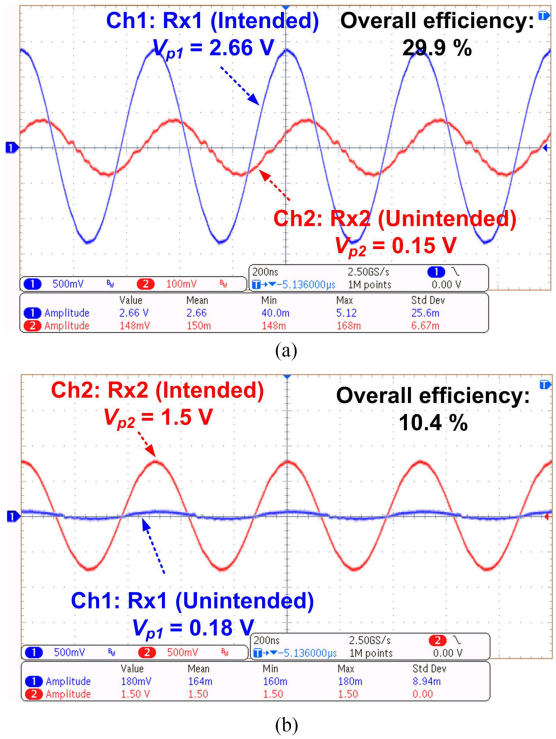

Fig. 6. Measured transient waveforms for (a) intended Rx1 and unintended Rx2 and (b) unintended Rx1 and intended Rx2 with the experimental setup in Fig. 3. The Rx load, R_L, is 4.7 Ω for both Rx1 and Rx2.

B. Selective WPT With Three Rxs

In this section, we present the results with three Rxs (two intended Rxs and one unintended Rx). Fig. 8 shows the 3-D Tx coil array with the three Rx coils, which are specified in Table IV. Tx1–Tx3 and Rx1-Rx2 positions are the same as the previous experiments, as shown in Fig. 5(a), while Rx3 is newly added at (80, 80, 60 mm) with 90° rotation based on the x-axis (coil is parallel with the xz plane). The mutual inductances of Tx1–Tx3 with Rx1–Rx3 are given in Table V. The Rx load resistance R_L is 4.7 Ω for Rx1, Rx2, and Rx3. In this setup, three scenarios (combinations) for two intended Rxs and one unintended Rx are considered. The maximum Tx voltage is set to 8 V to simultaneously provide enough PDL to two intended Rxs. For the same reason, we choose the maximum PDL threshold of the unintended Rx, Γ_q, of 1 mW, while the minimum PDL threshold of each intended Rx, κ_q, is 5 mW.

Based on the proposed MFFNSO algorithm in Table II, the optimal Tx vectors for Tx1–Tx3 can be derived as $8\sin(\omega t)$ V, $8\sin(\omega t + 202°)$ V, and $4.3\sin(\omega t + 174°)$ V, respectively, for the unintended Rx1 and intended Rx2 and Rx3. The resulted PDLs for Rx1, Rx2, and Rx3 are measured as 0.29, 27.1, and 25.8 mW, respectively, as shown in Fig. 9(a). For unintended Rx2 and intended Rx1 and Rx3, the derived Tx vectors are $8\sin(\omega t)$ V, $2.7\sin(\omega t - 24°)$ V, and $8\sin(\omega t + 36.2°)$ V, respectively. In this scenario, the measured PDLs of Rx1, Rx2, and Rx3 are 138, 0.52, and 13.8 mW as shown in the measured transient waveforms of Rx1–Rx3 [see Fig. 9(b)]. The optimal Tx vectors for unintended Rx3 and intended Rx1 and Rx2 are calculated

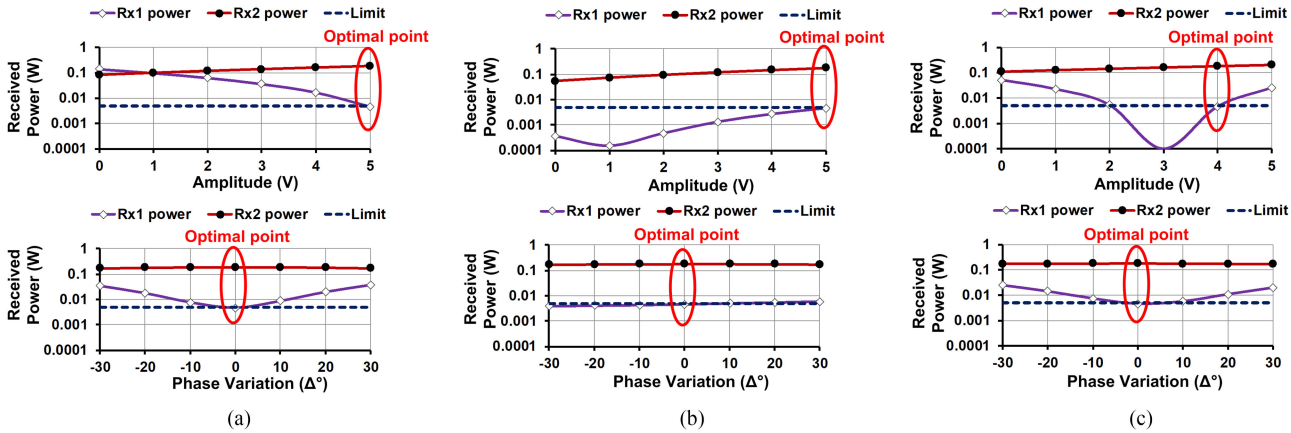

Fig. 7. Effectiveness of the proposed MFFNSO for the untended Rx1 and intended Rx2 in Fig. 4 with respect to the Tx vector variations of (a) Tx1, (b) Tx2, and (c) Tx3, from the optimal derived Tx vectors.

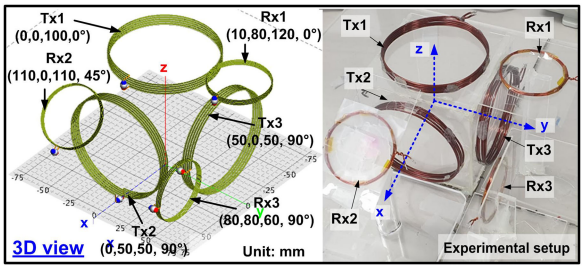

Fig. 8. Experimental setups for MFFNSO with three distributed Rx coils (Rx1–Rx3) with angular misalignments in the 3-D space. Tx1–Tx3 and Rx1–Rx2 positions are same in Fig. 5(a) while Rx3 is newly added at (80, 80, 60 mm) with 90° rotation based on the x-axis (coil is parallel with the xz plane).

based on MFFNSO, which are 8sin(ωt) V, 3.7sin(ωt + 218°) V, and 8sin(ωt + 24.6°) V for Tx1–Tx3, respectively. Even though the suppressed PDL on Rx3 (unintended) affects the PDL of Rx2 (intended) due to limited DoF with the three Tx coils, the proposed algorithm still can deliver 138 and 5.6 mW power to Rx1 and Rx2, while the significantly lower power of 0.19 mW is observed at the unintended Rx (i.e., Rx3), as shown in Fig. 9(c). The normalized 3-D magnetic field distributions from Tx1–Tx3 with Rx1–Rx3 for three scenarios are shown in Fig. 10 to support the measurement results, which are in line with the measurements shown in Fig. 9.

C. Further Investigation on Selectivity of MFFNSO

As discussed in Section III-E, in case that the intended and unintended Rxs are located in close proximity to each other, the MFFNSO algorithm may suffer from low selectivity because of the limited spatial resolution of the magnetic field, which is subject to the Tx array design (the number of coils, their structure and etc.), as noted in [38]. On the top of that, the increased mutual coupling between the intended and unintended Rxs makes the selective WPT more problematic. Motivated by this limitation, in this section, we delve into the selectivity performance of the proposed MFFNSO algorithm through simulation with three challenging configurations as shown in Fig. 11, which has three Tx coils and two Rxs with the same orientations.

In the first configuration, which corresponds to Fig. 11(a), the two Rxs are almost collocated with only 10 mm separation. Also, in the second case in Fig. 11(b), the two Rxs are deployed with a larger distance compared to the first topology, but they are still quite close to each other. In the third deployment in Fig. 11(c), the locations of the two Rxs are symmetric with respect to the origin. In the simulation, we used the same configurations listed in Table IV. In addition, as in Section IV-A, in each deployment, we considered the two opposite scenarios: 1) intended Rx1 and unintended Rx2 and 2) unintended Rx2 and intended Rx1. Further, the maximum allowable PDL of the unintended Rx is set to be 5mW, and the maximum amplitude of the Tx vectors are 5 V.

To evaluate the proposed algorithm, we compare its performances with the results using the optimal Tx voltage vectors obtained by exhaustive search, where the minimum step sizes of the Tx voltage amplitudes and phases are 0.001 V and 0.001°, respectively. The simulation results are summarized in Table VI, where the last two columns indicate the PDLs of the Rxs 1 and 2, respectively. First, we observe that the degradation in the PDL of the intended Rx by using MFFNSO relative to that of the exhaustive search is smaller than 1.3% for the same configuration and deployment. When it comes to the complexity, we can compare MFFNSO and exhaustive search in terms of the Big-O complexity measure, which is widely used to quantify the execution time required or the space used (e.g., in memory or on disk) by an algorithm [40]. According to [35], the computational complexity of MFFNSO is dominated by the optimization problem after SDR, which is of a worst-case complexity of $O(N^{4.5}\log(1/\epsilon))$ for a given accuracy $\epsilon > 0$. On the other hand, with the same accuracy requirement ϵ, the complexity of the exhaustive search is $O(1/\epsilon^N)$ [41]. Therefore, as the number of the Tx coils increases, the running time and space usage of the exhaustive increases exponentially, which is significantly larger compared to that of MFFNSO. Therefore, considering the time overhead, the proposed algorithm can be an effective alternative to achieve power selectivity.

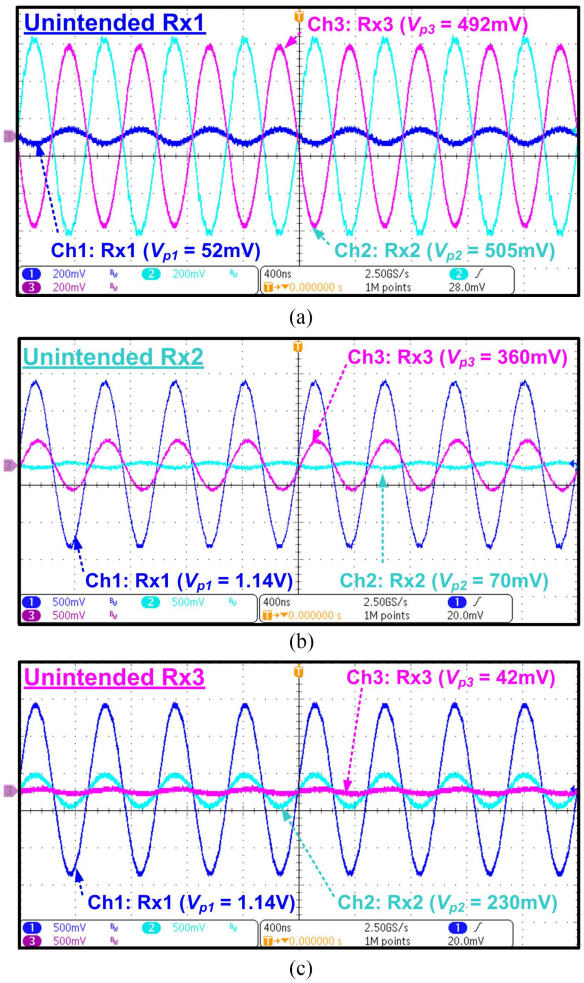

Fig. 9. Measured transient waveforms for (a) unintended Rx1 and intended Rx2 and Rx3, (b) unintended Rx2 and intended Rx1 and Rx3, and (c) unintended Rx3 and intended Rx1 and Rx2 with the experimental configurations in Fig. 8. The Rx load, R_L, is 4.7 Ω for Rx1–Rx3.

TABLE VI
SIMULATION RESULTS OF THREE RX DEPLOYMENTS

Test Case	Algorithm	Intended Rx	Rx1 PDL (mW)	Rx2 PDL (mW)
1	Proposed Algorithm (MFFNSO)	1	**6.97**	4.98
		2	4.49	**9.51**
	Exhaustive Search	1	**7.02**	4.94
		2	4.53	**9.63**
2	Proposed Algorithm (MFFNSO)	1	**8.51**	4.90
		2	4.99	**7.88**
	Exhaustive Search	1	**8.51**	4.90
		2	4.99	**7.89**
3	Proposed Algorithm (MFFNSO)	1	**168.07**	4.98
		2	4.89	**7.09**
	Exhaustive Search	1	**168.08**	4.98
		2	4.89	**7.09**

As shown in the table, for the all the three test topologies, both MFFNSO and exhaustive search satisfy the maximum allowable PDL of the unintended Rx, which is 5 mW. Moreover, comparing the three different topologies, as expected, the power ratios of the intended Rx to the unintended Rx are always smaller than two in the first two deployments because of the small separations between the two Rxs. These results indicate that it is difficult to achieve high power selectivity when the intended and unintended Rxs are tightly clustered. Moreover, in the last deployment, when Rx1 is the intended Rx, MFFNSO can deliver significantly higher power to Rx1 compared to Rx2. In contrast, if Rx2 is the intended Rx, it can only receive about 7.09 mW, while Rx1 receives about 4.89 mW. This PDL imbalance of the two scenarios with the different target Rxs is resulted from the fact that Rx1 is closer to Txs 2 and 3 compared to Rx2, as shown in Fig. 11(c). Nevertheless, we note that our proposed scheme always satisfies the PDL threshold of the unintended Rx. At the same, the intended Rx can achieve higher power compared to the unintended Rx even when switching the intended and unintended Rxs in all of the three test topologies. Also, in case that the intended and unintended Rxs have a large enough interseparation as in the experiments in the previous subsections, our proposed algorithm can provide highly selective WPT. However, to further improve our scheme and overcome the issues observed in the extreme scenarios investigated in this section, we can consider Tx arrays with more number of coils and different structures as noted in [37], which would be our potential extension in the future.

V. DISCUSSIONS

MFFNSO has been presented for the selective WPT system to simultaneously support the multiple intended receives (Rxs) in the presence of multiple unintended Rxs. The simulated and experimental results show that the proposed MFFNSO can successfully deliver the power to the multiple intended Rxs while limiting the received power at the unintended Rxs using the optimized precoding method.

Even though the MFF techniques are widely utilized to power one or multiple Rxs for the higher power transfer efficiency when the Rxs are distributed in the 3-D space [7], [8], [21]–[31], there have been few MFF techniques for the power selectivity issue limiting the received power in the unintended Rxs. However, the MFF-based WPT with selectivity has advantages in that the complex circuitries for the control can be implemented only to the Tx, while the Rx does not require complicated control. Considering the limited allowable frequency bands for the adaptive frequency-based power selectivity due to the physical or regulatory constraints, the MFF techniques become a more effective WPT method when the numbers of intended and unintended Rxs are increased in the system. In addition, it potentially provides the physical security of data telemetries for the uplink combined by the data modulation techniques, such as ASK, FSK, or PSK [42]–[44].

In [16], the MFF algorithm was proposed to limit the power leakage to the unintended Rx with multiple Tx array. To be specific, they formulated a non-convex optimization problem for the

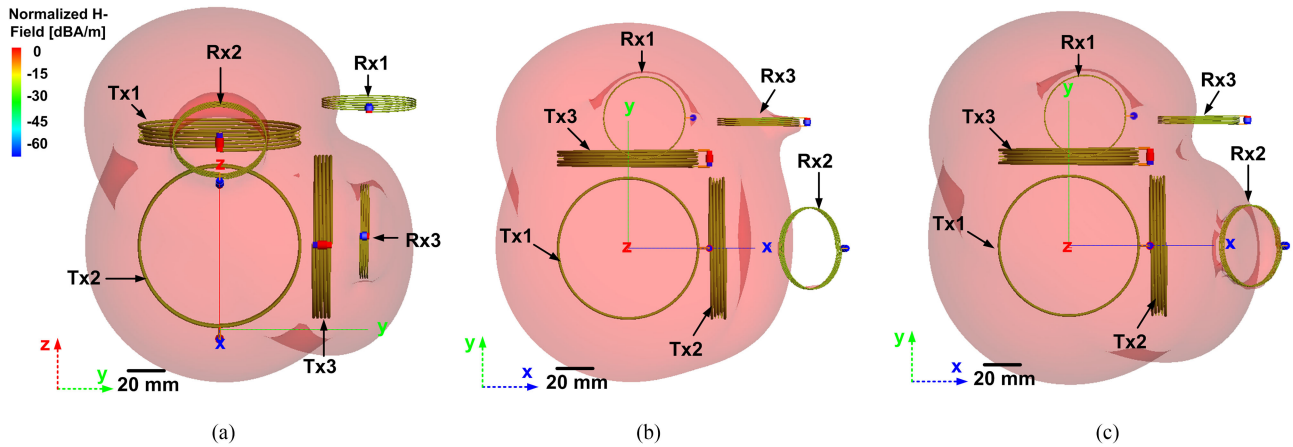

Fig. 10. Normalized 3-D magnetic field distributions from Tx1 to Tx3 for (a) unintended Rx1 and intended Rx2 and Rx3, (b) unintended Rx2 and intended Rx1 and Rx3, and (c) unintended Rx3 and intended Rx1 and Rx2.

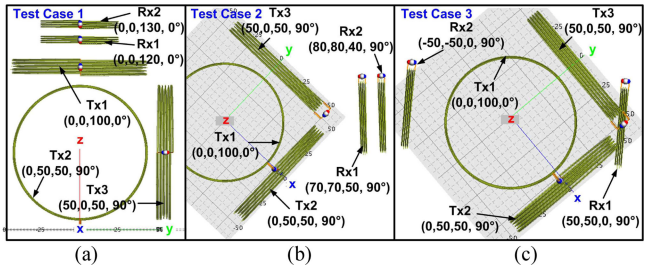

Fig. 11. Case studies for three different Rx positions. (a) Test case 1: Rx1 = (0, 0, 120 mm), Rx2 = (0, 0, 130 mm) without angular misalignment. (b) Test case 2: Rx1 = (70, 70, 50 mm), Rx2 = (80, 80, 40 mm) with the 90° angular misalignment along with the *xy* plane. (c) Test case 3: Rx1 = (50, 50, 0 mm), Rx2 = (−50, −50, 0 mm) with the 90° angular misalignment along with the *xy* plane.

selective WPT through precoding, and they theoretically proved that the optimal solution (source voltages) can be effectively obtained by SDR. In addition, in [31], the authors improved the robustness of their precoding algorithm in [16] assuming more generalized configurations with multiple unintended Rxs. However, they still assumed a single intended Rx, which is not appropriate to support multiple devices simultaneously, as noted in [8]–[11], [13], and [27]. Moreover, the mutual couplings between Rxs were ignored in [16] and [32]. However, as emphasized in [27], different from RF-based beamforming systems, which is focused only on radiation between Tx and Rxs, signal reflection occurs even between Rxs in MRC-based systems. Such reflected signals can be combined constructively or destructively depending on the phase differences. For this reason, the applicability of [16] and [32] is limited in general (e.g., multiple Rxs in proximity). Furthermore, in [16] and [32], the theoretical analysis without experimental validation was focused. On the other hand, the work in [22] showed through experimental results that selective MFF can be used to maximize the power transfer to a selected Rx, while leakage to the other device is suppressed. However, they only presented simulation and experimental data without proposing a specific method to find the optimal precoding weights (e.g., source voltages) for simultaneous MFF and null-steering, which incurs time consuming exhaustive search and limited scalability. To the best of our knowledge, this article, MFFNSO, is the first to consider the generalized solution exploiting MFF and null-steering for selective WPT systems with multiple intended and unintended Rxs distributed in the 3-D space, and has been verified by both the simulation and measurement results.

VI. Conclusion

In this article, we have investigated an optimization problem in MRC WPT with selective spatial distribution of energy using MFFNSO, which is subject to circuit constraints. We have formulated the optimization problem of selective WPT, where the total PDL at the intended Rxs is maximized, while the PDL at the individual unintended Rx is kept below certain thresholds. We have proposed a method to readily obtain the optimal Tx voltage vector by SDR and rank reduction based on randomization. The proposed method has been validated through simulation and experiments. The EM simulation results have indicated distinctive field intensity distributions of the intended and unintended Rxs. Furthermore, the experimental results have demonstrated the effectiveness and robustness of our proposed algorithm in contrast to the poor selectivity performances of the maximum PDL and the selective Tx driving methods.

References

[1] K. Finkenzeller, *RFID-Handbook*, 2nd ed. Hoboken, NJ, USA: Wiley, 2003.
[2] C.-S. Wang, O. H. Stielau, and G. A. Covic, "Design considerations for a contactless electric vehicle battery charger," *IEEE Trans. Ind. Electron.*, vol. 52, no. 5, pp. 1308–1314, Oct. 2005.
[3] B. Lee *et al.*, "An implantable peripheral nerve recording and stimulation system for experiments on freely moving animal subjects," *Sci. Rep.*, vol. 8, pp. 1–12, Apr. 2018.
[4] J. Huh, S. W. Lee, W. Y. Lee, G. H. Cho, and C. T. Rim, "Narrow-width inductive power transfer system for online electrical vehicles," *IEEE Trans. Power Electron.*, vol. 26, no. 12, pp. 3666–3679, Dec. 2011.

[5] G. A. Covic, J. T. Boys, M. L. G. Kissin, and H. G. Lu, "A three-phase inductive power transfer system for roadway-powered vehicles," *IEEE Trans. Ind. Electron.*, vol. 54, no. 6, pp. 3370–3377, Dec. 2007.
[6] B. Lee, D. Ahn, and M. Ghovanloo, "Three-phase time-multiplexed planar power transmission to distributed implants," *IEEE J. Emerg. Sel. Topics Power Electron.*, vol. 4, no. 1, pp. 263–272, May 2015.
[7] J. Jadidian and D. Katabi, "Magnetic MIMO: How to charge your phone in your pocket," in *Proc. ACM MobiCom*, 2014, pp. 495–506.
[8] S. Kisseleff, I. F. Akyildiz, and W. H. Gerstacker, "Magnetic induction-based simultaneous wireless information and power transfer for single information and multiple power receivers," *IEEE Trans. Commun.*, vol. 65, no. 3, pp. 1396–1410, Mar. 2017.
[9] A. Kurs, A. Karalis, R. Moffatt, J. D. Joannopoulos, P. Fisher, and M. Soljacic, "Wireless power transfer via strongly coupled magnetic resonances," *Sci. Express*, vol. 317, pp. 83–86, Jul. 2007.
[10] M. Pinuela, D. C. Yates, S. Lucyszyn, and P. D. Mitcheson, "Maximizing DC-to-load efficiency for inductive power transfer," *IEEE Trans. Power Electron.*, vol. 28, no. 5, pp. 2437–2447, May 2013.
[11] B. Lee, P. Yeon, and M. Ghovanloo, "A multi-cycle Q-modulation for dynamic optimization of inductive links," *IEEE Trans. Ind. Electron.*, vol. 63, no. 8, pp. 5091–5100, Aug. 2016.
[12] J. Kang *et al.*, "Toward secure energy harvesting cooperative networks," *IEEE Commun. Mag.*, vol. 53, no. 8, pp. 114–21, Aug. 2015.
[13] Q. Liu, K. S. Yildirim, P. Pawlczak, and M. Warnier, "Safe and secure wireless power transfer networks: Challenges and opportunities in RF-based systems," *IEEE Commun. Mag.* vol. 54, no. 9, pp. 74–79, Sep. 2016.
[14] N. Zhao, F. R. Yu, and V. C. M. Leung, "Opportunistic communications in interference alignment networks with wireless power transfer," *IEEE Wireless Commun.*, vol. 22, no. 1, pp. 88–95, Feb. 2015.
[15] F. Zhu, F. Gao, M. Yao, and H. Zou, "Joint information- and jamming beamforming for physical layer security with full duplex base station," *IEEE Trans. Signal Process.*, vol. 62, no. 24, pp. 6391–6401, Dec. 2014.
[16] H. Sun, H. Lin, F. Zhu, and F. Gao, "Magnetic resonant beamforming for secured wireless power transfer," *IEEE Signal Process. Lett.*, vol. 24, no. 8, pp. 1179–1177, Aug. 2017.
[17] Z. Zhang, K. Chau, C. Qiu, and C. Liu, "Energy encryption for wireless power transfer," *IEEE Trans. Power Electron.*, vol. 30, no. 9, pp. 5237–5246, Sep. 2015.
[18] Z. Zhang, K. Chau, C. Liu, and C. Qiu, "Energy-security based contactless battery charging system for roadway powered electric vehicles," in *Proc. IEEE PELS Workshop Emer. Technol., Wireless Power*, Jun. 2015, pp. 1–6.
[19] L. Ji, L. Wang, and C. Liao, "A new method of encryption wireless energy transmission for EV in the smart grid," *CES Trans. Elect. Mach. Syst.*, vol. 1, no. 4, pp. 405–410, Dec. 2017.
[20] E. Ahene, M. Ofori-Oduro, and B. Agyemang, "Secure energy encryption for wireless power transfer," in *Proc. IEEE 7th Int. Adv. Comput. Conf.*, Jul. 2017, pp. 199–204.
[21] D. Ahn and S. Hong, "Effect of coupling between multiple transmitters or multiple receivers on wireless power transfer," *IEEE Trans. Ind. Electron.*, vol. 60, no. 7, pp. 2602–2613, Jul. 2013.
[22] B. H. Waters, B. J. Mahoney, V. Ranganathan, and J. R. Smith, "Power delivery and leakage field control using an adaptive phased array wireless power system," *IEEE Trans. Power Electron.*, vol. 30, no. 11, pp. 6298–6309, Nov. 2015.
[23] B. H. Choi, J. H. Kim, J. P. Cheon, and C. T. Rim, "Synthesized magnetic field focusing using a current-controlled coil array," *IEEE Magn. Lett.*, vol. 7, Jan. 2016, Art. no. 6501504.
[24] K. Hamano, K. Ohtsuka, R. Tanaka, and K. Nishikawa, "4× 1 multi-input single-output magnetic resonance beamforming wireless power transfer system," in *Proc. Int. IEEE Appl. Comput. Electromagn. Soc. Symp.*, Aug. 2017, pp. 1–2.
[25] B.-H. Choi, B.-C. Park, and J.-H. Lee, "Near-field beamforming loop array for selective wireless power transfer," *IEEE Microw. Wireless Compon. Lett.*, vol. 25, no. 11, pp. 748–750, Nov. 2015.
[26] G. Yang, M. R. V. Moghadam, and R. Zhang, "Magnetic MIMO signal processing and optimization for wireless power transfer," *IEEE Trans. Signal Process*, vol. 65, no. 11, pp. 2860–2874, Jun. 2017.
[27] S. Kisseleff, I. F. Akyildiz, and W. Gerstacker, "Beamforming for magnetic induction based wireless power transfer systems with multiple receivers," in *Proc. IEEE Global Commun. Conf.*, Feb. 2016, pp. 1–7.
[28] M. R. V. Moghadam and R. Zhang, "Multiuser wireless power transfer via magnetic resonant coupling performance analysis, charging control, and power region characterization," *IEEE Trans. Signal Inf. Process. Netw.*, vol. 2, no. 1, pp. 72–83, Mar. 2016.
[29] L. Shi, Z. Kabelac, D. Katabi, and D. Perreault, "Wireless power hotspot that charges all of your devices," in *Proc. ACM MobiCom*, Sep. 2015, pp. 2–13.
[30] H. Lang, A. Ludwig, and C. D. Sarris, "Convex optimization of wireless power transfer systems with multiple transmitters," *IEEE Trans. Antennas Propag.*, vol. 62, no. 9, pp. 4623–4636, Sep. 2014.
[31] T. Arakawa *et al.*, "Optimizing wireless power transfer from multiple transmit coils," *IEEE Access*, vol. 6, pp. 23828–23838, 2018.
[32] H. Sun, F. Zhu, H. Lin, and F. Gao, "Robust magnetic resonant beamforming for secured wireless power transfer," *IEEE Signal Process. Lett.*, vol. 25, no. 8, pp. 1226–1230, Jun. 2018.
[33] Z. Luo, W. Ma, A. M. So, Y. Ye, and S. Zhang, "Semidefinite relaxation of quadratic optimization problems," *IEEE Signal Process. Mag.*, vol. 27, no. 3, pp. 20–34, Apr. 2010.
[34] M. Grant, S. Boyd, and Y. Ye, CVX: MATLAB software for disciplined convex programming, 2009. [Online]. Available: http://www. stanford. edu/∼boyd/cvx
[35] Y. Huang and D. P. Palomar, "Randomized algorithms for optimal solutions of double-sided QCQP with applications in signal processing," *IEEE Trans. Signal Process.*, vol. 62, no. 5, pp. 1093–1108, Mar. 2014.
[36] A. Khisti and G. W. Wornell, "Secure transmission with multiple antennas I: The MISOME wiretap channel," *IEEE Trans. Inf. Theory*, vol. 56, no. 7, pp. 3088–3104, Jul. 2010.
[37] H. Weingarten, Y. Steinberg, and S. Shamai, "The capacity region of the Gaussian multiple-input multiple-output broadcast channel," *IEEE Trans. Inf. Theory*, vol. 52, pp. 3936–3964, Sep. 2006.
[38] B. Zhao, N.-C. Kuo, and A. M. Niknejad, "A gain boosting array technique for weakly-coupled wireless power transfer," *IEEE Trans. Power Electron.*, vol. 32, no. 9, pp. 7130–7139, Sep. 2017.
[39] A. Feko, "Altair engineering," 2018. [Online]. Available: http://altairhyperworks.com/product/FEKO
[40] S. Devi, K. Selvam, and S. Rajagopalan, "An abstract to calculate big O factors of time and space complexity of machine code," in *Proc. Int. Conf. Sustain. Energy Intell. Syst.*, Jul. 2011, pp. 844–847
[41] Z. B. Zabinsky, *Stochastic Adaptive Search for Global Optimization*. New York, NY, USA, Springer-Verlag, 2003.
[42] T. J. Lee, C. L. Lee, Y. J. Ciou, C. C. Huang, and C. C. Wang, "All-MOS ASK demodulator for low-frequency applications," *IEEE Trans. Circuit Syst. II, Express Briefs*, vol. 55, no. 5, pp. 474–478, May 2008.
[43] Z. Lu and M. Sawan, "An 8 Mbps data rate transmission by inductive link dedicated to implantable devices," in *Proc. Dig. Tech. Papers IEEE Int. Circuit Syst. Conf.*, May 2008, pp. 3057–3060.
[44] Y. Hu and M. Sawan, "A fully integrated low-power BPSK demodulator for implantable medical devices," *IEEE Trans. Circuit Syst. I, Reg. Papers*, vol. 52, no. 12, pp. 2552–2562, Dec. 2005.

Haejoon Jung (S'10–M'14) received the B.S. degree from Yonsei University, Seoul, South Korea, in 2008, and the M.S. and Ph.D. degrees from the Georgia Institute of Technology, Atlanta, GA, USA, in 2010 and 2014, respectively.

He has been an Assistant Professor with Incheon National University, Incheon, South Korea, since 2016. From 2014 to 2016, he was a Wireless Systems Engineer with Apple, Cupertino, CA, USA. His research interests fall into the broad areas of communication theory, wireless communications, wireless power transfer, and statistical signal processing.

Byunghun Lee (S'11–M'17) received the B.S. degree from Korea University, Seoul, South Korea, in 2008, the M.S. degree from the Korea Advanced Institute of Technology (KAIST), Daejeon, South Korea, in 2010, and the Ph.D. degree in electrical and computer engineering from the Georgia Institute of Technology, Atlanta, GA, USA, in 2017.

From 2010 to 2011, he worked on wireless power transfer systems for electric vehicles at KAIST as a Research Engineer. He is currently an Assistant Professor with the Department of Electrical Engineering, Incheon National University, Seoul, South Korea, and the Director of INU-Wireless Lab.